Precise and Efficient Phototheranostics: Molecular Engineering of Photosensitizers with Near-Infrared Aggregation-Induced Emission for Acid-Triggered Nucleus-Targeted Photodynamic Cancer Therapy

Zhijun Zhang, Wenhan Xu, Peihong Xiao, Miaomiao Kang, Dingyuan Yan, Haifei Wen, Nan Song, Lei Wang, Dong Wang,* and Ben Zhong Tang*

Dr. Z. Zhang, Dr. P. Xiao, Dr. M. Kang, Dr. D. Yan, H. Wen, Dr. N. Song, Prof. L. Wang, Prof. D. Wang
Center for AIE Research, Shenzhen Key Laboratory of Polymer Science and Technology, Guangdong Research Center for Interfacial Engineering of Functional Materials, College of Material Science and Engineering, Shenzhen University, Shenzhen 518061, P. R. China
E-mail: wangd@szu.edu.cn

Dr. Z. Zhang, Dr. P. Xiao, Dr. M. Kang, Dr. D. Yan, Dr. N. Song
Key Laboratory of Optoelectronic Devices and Systems of Ministry of Education and Guangdong Province, College of Optoelectronic Engineering, Shenzhen University, Shenzhen 518060, China

W. Xu, Prof. B. Z. Tang
Hong Kong Branch of Chinese National Engineering Research Center for Tissue Restoration and Reconstruction, Department of Chemistry, The Hong Kong University of Science and Technology, Clear Water Bay, Kowloon, Hong Kong 999077, China
E-mail: tangbenz@ust.hk

Keywords: aggregation-induced emission, photodynamic therapy, NIR emission, molecular engineering, nucleus-targeted theranostics

Abstract

Phototheranostics involving both fluorescence imaging (FLI) and photodynamic therapy (PDT) has been recognized to be potentially powerful for cancer treatment by virtue of various intrinsic advantages. However, the state-of-the-art materials in this area are still far from ideal towards practical applications, owing to their respective and collective drawbacks, such as inefficient imaging quality, inferior reactive oxygen species (ROS) production, the lack of subcellular-targeting capability, and dissatisfactory theranostics delivery. In this contribution, these shortcomings are successfully addressed through the integration of finely engineered photosensitizers having aggregation-induced emission (AIE) features and well tailored nanocarrier system. The yielded AIE NPs simultaneously exhibit broad absorption in visible light region, bright near-infrared fluorescence emission, extremely high ROS generation, as well as tumor lysosomal acidity-activated and nucleus-targeted delivery functions, making them dramatically promising for precise and efficient phototheranostics. Both in vitro and in vivo evaluations show that the presented nanotheranostic system bearing excellent photostability and appreciable biosecurity well performed in FLI-guided photodynamic cancer therapy. This study thus not only extends the applications scope of AIE nanomaterials, but also offers useful insights into constructing a new generation of cancer theranostics.

Introduction

Cancer diagnostics and therapeutics research has received significant attention over the past few decades. As one of numerous advances in this area, phototheranostics that performs diagnosis and

concurrent in situ therapy via light initiation has emerged as a promising noninvasive theranostic protocol to surmount cancers.[1] Among diverse light-triggered diagnostic/therapeutic techniques, fluorescence imaging (FLI) associated with photodynamic therapy (PDT) have being attracted tremendous scientific interest due to their combined merits of high diagnostic sensitivity and temporal resolution in view of FLI, and high therapeutic effectiveness and controllability in view of PDT.[2] Various organic and inorganic materials, nano-sized ones in particular, have been continuously exploited to construct the phototheranostic systems involving both FLI and PDT nowadays.[3] However, previously reported systems exhibit their respective and collective drawbacks including inefficient imaging quality, inferior photosensitizing property, the lack of subcellular-targeting capability and dissatisfactory theranostics delivery,[4] all those severely hamper their preclinical research and clinical applications. In particular, the former two shortcomings have been long-term unresolved issues. Most of the conventional photosensitizers (PSs) are hydrophobic and inclined to aggregate in a physiological environment, resulting in fluorescence quenching and insufficient reactive oxygen species (ROS) production owing to the aggregation-caused quenching (ACQ) phenomenon, which was caused by strong intermolecular π-π stacking and other amplified nonradiative pathways in aggregates.[5] Evidently, the development of precise and efficient phototheranostics by means of FLI-guided PDT is an appealing yet significantly challenging task.

As an anti-ACQ concept, the emergence of aggregation-induced emission (AIE) could trigger state-of-the-art development of FLI-guided PDT. AIE refers to a unique phenomenon that some organic molecules with twisted conformation are weakly emissive in dilute solutions but can emit bright fluorescence in aggregated states through a mechanism of the restriction of intramolecular motions (RIM).[6] The AIE properties make AIE luminogens (AIEgens) ideal for fabrication of fluorescent nanoparticles (NPs) with ultrahigh brightness and photobleaching threshold.[7] Attractively, precise molecular engineering could also endow AIEgens with high-efficiency photosensitizing feature in aggregated states, even superior to many commercial PSs.[8] More importantly, AIE NPs show exceptionally linear loading percentage-dependent increase in brightness and photosensitization, which distinguishes them from ACQ NPs that exhibit compromised brightness and photosensitization at high loadings. Additionally, the integration of different functions within a single kind of AIEgen represents a facile strategy for theranostic NPs with great simplicity and reproducibility different from traditional theranostic systems containing complicated components.[9] These distinct features make AIEgens a superb option to build phototheranostics. Nevertheless, current situation of AIEgens in FLI-guided PDT is still far from ideal, and some major problems remain to be solved. So far, the reported AIE PSs usually show maximum emission peaks in the visible light range.[10] Aiming to the practical/clinical applications, the development of AIE PSs with intense emission in near-infrared (NIR) region (beyond 700 nm) is highly desirable, by virtues of their minimal tissue absorption, reduced light scattering, slight photodamage to biological structures, ignorable autofluorescence of normal tissues, as well as the resulted relatively deeper tissue penetration.[11] Moreover, the ROS generation efficiency of the previously developed AIE PSs is still need to be further improved. Therefore, precise molecular engineering of AIE PSs affording both bright NIR emission and supremely high ROS production would be unambiguously conducive to efficient phototheranostics.

Except for the promotion of PS properties, it has been demonstrated that appropriate intracellular location and effective delivery of PS are of vital importance for final PDT outcomes. ROS has an instantaneous lifetime of less than 40 ns and a short diffusion radius about 20 nm, which caused the effective damage area of ROS to be restricted to the immediate vicinity of the PS in subcellular

scale.[12] Due to the critical biological effects of diverse subcellular compartments, it is generally acknowledged the dysfunction or destruction of any of these specific parts would induce cell death in the most essential way.[13] To this end, a variety of organelle-targeted nanodelivery systems that can precisely transport PS to subcellular sites such as mitochondria, lysosomes and endoplasmic reticulum, have been extensively exploited to realize enhanced PDT effects.[14] Very recently, nucleus-targeted drug delivery strategy was also employed to ship PS for extraordinarily amplifying the PDT potency, considering that cell nucleus is a much more sensitive and ideal site for photodynamic damage as compared with other subcellular organelles.[15] Thereupon, tactics that involve the specific delivery of PS towards key locations have been developed as "precision medicine" for subcellular-level tumor treatments.[4c] Furthermore, an ideal organelle-targeted carrier should stay inert during the blood circulation while specifically be activated in tumor microenvironment or inside cancer cells by responding to inherent biological stimuli including pH, temperature, enzymes, redox potential, etc.[16] Among them, the acidic pH in the endo/lysosomes (pH 4-5) is of particular interest for designing acid-triggered nucleus-targeted nanovector systems.[17]

In this contribution, we reported an acid-triggered nucleus-targeted phototheranostic nanosystem based on a NIR AIE PS for precise and efficient photodynamic cancer therapy. The NIR-emissive AIE PS with extremely high ROS generation efficiency was finely engineered. Acid-active TAT peptide was tactfully employed for translocating the AIE NPs into the nuclear regions and made the produced ROS accumulated in the nuclei. The ingenious combination of high-performance cargos and tailored vehicles endowed the AIE NPs with superior versatility. Both in vitro and in vivo studies proved that the phototheranostic nanomaterial with appreciable biocompatibility exhibited excellent performance in NIR FLI-guided PDT. This study will offer new insights into the construction of advanced phototheranostics by making the best of both theranostic molecules and nanodelivery systems.

Results and Discussion

Generally, the integration of strong electron donating-accepting (D-A) interaction into the conjugated fluorophores could remarkably facilitate intramolecular charge transfer (ICT), and thereout resulting in lower electronic bandgaps, as well as longer absorption and emission wavelengths.[18] As illustrated in Scheme 1A, the designed compounds TTMN, TPE-TTMN, TPE-TTMN-OMe and TPE-TTMN-TPA comprised by triphenylamine (TPA) segment (working as D), thiophene fragment (D and π-bridge), methoxyl group (D), carbon-carbon double bond (π-bridge) and two cyano units (A), showed extremely high D-A strength and extended π-conjugation with varying degrees. The orderly increased D-A extent ranging from TTMN, TPE-TTMN, TPE-TTMN-OMe to TPE-TTMN-TPA, implies the red-shifts of both absorption and emission wavelengths in this order. In this design, freely rotated molecular rotators constitute all those presented compounds, and the sufficient rotations could consume exciton energy upon photoexcitation, thus allowing weak or no emission when dissolved in solution. On the other hand, the highly twisted conformation of tetraphenylethylene (TPE) and TPA segments could efficaciously prevent the fluorescence quenching in aggregation state benefiting from the significantly enlarged intermolecular distance and reduced intermolecular π-π interaction. Apparently, these structural features would endow these compounds with AIE characteristics and longer wavelengths of absorption and emission. On the other hand, enhancement of the D-A strength is also one of the key protocols to boost ROS generation efficiency of PS, due to that a high D-A effect could induce the decrease of energy gap between the lowest

excited singlet (S1) and the lowest excited triplet (T1), which favors the intersystem crossing (ISC) process and further promotes the cytotoxic ROS production.[10a] Besides, it is believed that ISC process can also be elevated by the existence of heteroatom components.[19] Accordingly, it seems reasonable to infer that compound TPE-TTMN-TPA bearing the strongest D-A interaction and maximum heteroatomic number (O, S and N) would be the best candidate for phototheranostics construction in terms of both emission wavelength and ROS genaration efficiency compared to other counterparts.

To verify these hypotheses and investigate the structure-property relationship of the presented compounds, we started with the synthesis. As depicted in Scheme S1 (Supporting Information), TTMN was facilely prepared by two-step reactions. The primary step was the synthesis of compound **1** by Suzuki reaction of 4-bromo-*N*,*N*-diphenylaniline with (5-formylthiophen-2-yl)boronic acid in the presence of Pd catalyst, then TTMN was produced by Knoevenagel condensation reaction between compound **1** and malononitrile. As substituted derivatives of TTMN, other three AIEgens (TPE-TTMN, TPE-TTMN-OMe and TPE-TTMN-TPA) were smoothly synthesized by four steps. Reaction between (2-(4-bromophenyl)ethene-1,1,2-triyl)tribenzene and anilines was conducted in toluene using $Pd_2(dba)_3$ as catalyst, leading to the intermediate product **2**. Buchwald-Hartwig coupling of product **2** with 1-bromo-4-iodobenzene then proceeded to yield bromated compound **3**. Finally, TPE-TTMN, TPE-TTMN-OMe and TPE-TTMN-TPA were readily obtained through successive Suzuki-Miyaura coupling and Knoevenagel condensation reactions of (5-formylthiophen-2-yl)boronic acid, compound **3** and malononitrile. The structures of finnal products and intermediate products were characterized with satisfactory results.

Compounds TTMN, TPE-TTMN, TPE-TTMN-OMe and TPE-TTMN-TPA exhibit good solubility in common organic solvents. Benefiting from the orderly enhancement of D-A strength from TTMN to TPE-TTMN-TPA, their solutions in acetonitrile (ACN) displayed gradually red-shifted maximum absorption peaks ranging from 485 to 539 nm (Figure 1A). These relatively long absorption maxima locating in the range of visible light which shows less damage to biological system against UV light allow higher penetration depth of excitation sources. The study of AIE property was performed in ACN/water mixtures with different water fractions, which enable certain extent of solute aggregation. It was observed that all those four compounds exhibited rather faint photoluminescences (PL) in ACN solutions, and the maximum emissions are peaked at 662, 656, 667 and 685 nm, respectively, with the highest quantum yields determined to be 0.32%. It it thus reationlized that the energy of the excited state upon photoexcitation is efficiently consumed by the strong rotation of freely rotated molecular moieties in solution state, thus providing weak emissions. With raising fraction of water in the ACN/water mixtures, in all cases of four compounds, the PL intensities gradually increase because of the nanoaggregation formation (Figure 1B and 1C; Figure S1, Supporting Information). Comparing with the solution state, their emission maxima were respectively red-shifted to 664, 670, 685 and 712 nm in aggregates, and the PL intensities were remarkably enhanced to about 12-, 104-, 129- and 41-fold upon aggregation, definitely indicating their typical AIE characteristics. Importantly, the emission peak of TPE-TTMN-TPA reached the NIR region in aggregate state, implying the potential possibility of TPE-TTMN-TPA in the application of NIR imaging. Moreover, the PL spectra of these AIEgens in solid state were peaked at 691, 694, 722 and 770 nm respectively (Figure 1D), exhibiting relatively high quantum yields ranging from 1.4% to 26.2%, as well as lifetimes ranging from 5.94 to 7.6 ns (Figure 1E; Table S1, Supporting Information). To get a deeper insight into the determined photophysical properties, density functional theory (DFT) calculations were implemented using the

B3LYP/6-31G(d,p) basis set. As shown in Figure S2 (Supporting Information), the electron clouds of the highest occupied molecular orbital (HOMO) are mainly located on triphenylamine fragment and/or methoxyl moiety, while the lowest unoccupied molecular orbitals (LUMO) are dominated by the orbitals of cyano units (A), displaying the intrinsic ICT character and D-A structural feature. From AIEgen TTMN to TPE-TTMN-TPA, the energy levels of HOMOs and LUMOs are both lowered, accompanying with the orderly decreased values of calculated energy gaps (2.6, 2.41, 2.34 and 2.21 eV), which are in good accordance with experimental data involving both their long absorption and emission wavelengths with redshifts from TTMN to TPE-TTMN-TPA. Next, the ROS generation efficiencies of these presented AIEgens were evaluated by using DCFH as an indicator, whose green fluorescence can be triggered upon irreversible reaction with ROS. As shown in Figure 1F, DCFH alone was almost non-emissive upon light illumination, while the fluorescence intensity of DCFH at 525 nm enhanced sharply along with the increasing of the irradiation time in the presence of AIEgens with an extremely low concentration of 2×10^{-7} M. Notably, in the presence of TPE-TTMN-TPA, the emission intensity of DCFH reached nearly 600-fold after 10 min white light irradiation, showing much superior ROS production efficiency than those of TTMN (306-fold), TPE-TTMN (430-fold) and TPE-TTMN-OMe (500-fold). Excitedly, the ROS generation ability of TPE-TTMN, TPE-TTMN-OMe and TPE-TTMN-TPA even exceeded Rose Bengal which is the most widely used and reputable PS for PDT, as the emission intensity of DCFH only increased 372-fold in the presence of Rose Bengal under the same conditions. The highly efficient ROS generation can be attributed to their small singlet-triplet energy gaps (0.008 eV for TPE-TTMN, 0.011 eV for TPE-TTMN-OMe and 0.005 eV for TPE-TTMN-TPA), which favor the ISC pathway and considerably improve the yield of the triplet excited state. Under this consideration, TPE-TTMN-TPA bearing the smallest singlet-triplet energy gap resulting from the strongest D-A effect and most heteroatoms in structure is evidently rationalized to display the highest ROS generation efficiency.

With high-performance AIE PS in hand, the fabrication of biocompatible and well-dispersible nucleus-targeted nanodelivery platforms for satisfying the biological applications in aqueous media and implementing the nuclear photosensitization of PS was next conducted. TAT peptide, as a type of nuclear localization signal peptides, can be recognized by the nuclear pore complexes and thus has been utilized as an exceptionally efficient “locomotive” for efficiently transporting various cargos from the cytosol into cell nuclei.[20] However, TAT is a highly cationic peptide rich in lysine and arginine amino acids, and its positive charge can cause strong nonspecific interactions in the bloodstream, making TAT-decorated cargos inaccessible to in vivo applications.[21] The primary amines of lysine in TAT are considered as the main cause of nonspecificity, but they also play a key role in nuclear localization function.[22] Thankfully, some β-carboxylic amides are very stable at neutral pH but easily hydrolyzable at acidic pH to regenerate the corresponding amines.[23] Inspired by this, lysine residue amines of TAT were functionalized with succinic anhydride (SA) into succinic anhydride-modified TAT (SA-TAT), in which the succinyl amides could remain steady under normal physiological pH environment but break quickly responding to endo/lysosomal acidity.[22,24] The resulting SA-TAT was further modified to the terminal of maleimide-end capped poly(ethylene glycol)-block-poly(lactic acid) (Mal-PEG-PLA) for offering the amphiphilic copolymer denoted as SA-TAT-PEG-PLA. The acid-triggered nucleus-targeted nanocarriers were fabricated via coassembly of SA-TAT-PEG-PLA and PEG-PLA with a mole ratio of 15: 85, and further utilized to encapsulate hydrophobic TPE-TTMN-TPA through a nanoprecipitation method to obtain TPE-TTMN-TPA-loaded NPs (abbreviated as T4-NPs) for the following theranostic studies (Scheme 1B). As shown in

Figure 2A, the as-prepared T4-NPs had an average diameter of 71 nm determined by dynamic light scattering (DLS) measurement at pH 7.4. The size rightly located in the range of 50-100 nm, which are known to be optimal sizes for passive accumulation into tumor tissues by enhanced permeability and retention (EPR) effect. Transmission electron microscopy (TEM) image revealed T4-NPs possessed spherical nanostructures with the diameter ranging from 50 to 70 nm (Figure 2B), which was smaller than the hydrodynamic diameter value detected by DLS, possibly ascribing to the absence of hydration layer on the surface of the NPs. Furthermore, the zeta potential of T4-NPs was determined to be -15.5 mV under pH 7.4 condition (Figure 2D). Notably, no obvious variations of the partical size and the absorption of T4-NPs were observed after storage in PBS or 10% FBS at ambient condition for one week (Figure S3, Supporting Information). The negative surface charge and excellent colloidal stability of NPs would significantly contribute to the long blood circulation and minimal reticuloendothelial system clearance. Moreover, it was observed that the afforded T4-NPs exhibited broad and strong absorption in visible region with maximum absorbance at 530 nm (Figure 2C), greatly facilitating their light harvesting efficiency. Noteworthily, T4-NPs exhibited a large Stokes shift (184 nm) and strong NIR fluorescence with the emission peak distinctly falling in the NIR region, indicating the tremendous potentials of T4-NPs for in vivo NIR FLI. Afterwards, the acid-activated behaviors of T4-NPs were investigated by combining multiple analysis methods. As illustrated in Figure 2D, incubation of T4-NPs at pH 5.0 lead to a dramatic transformation of the surface charge from negative to positive (+6.72 mV), which should be attributed to the acid-triggered cleavages of the amide bonds connected with negative succinyl shielding. Next, the internalization efficiency of T4-NPs into 4T1 cells was examined through fluorescence activated cell sorting (FACS) analysis after pretreatment of T4-NPs under different pH conditions (Figure 2E). As predicted, T4-NPs pretreated at pH 7.4 exhibited very slow cell intake, with only 25.9% of the 4T1 cells showing a barely measurable NIR fluorescence singal. In sharp contrast, T4-NPs pretreated at pH 5.0 exhibited ultra-strong cell uptake ability with the portion of positive cells acounting for 78.2%, as well as high mean fluorescence intensity (MFI) value (≈120) which was more than 4-fold higher as compared with that of T4-NPs pretreated at pH 7.4 (Figure S4, Supporting Information). In addition, to better clarify the acid-activated features, the nanocarriers coassembled from 15 mol% TAT-PEG-PLA (without SA shielding) and 85 mol% PEG-PLA were also constructed to load TPE-TTMN-TPA molecules, and the yielded NPs (defined as T4-PNPs) were used as a positive control. Excitingly, the cellular uptake of T4-NPs (preactivation at pH 5.0) was very similar to that of T4-PNPs, implying the recovery of fully functioning TAT moieties on the NPs surface. In order to further confirm the acid-activated properties of T4-NPs, multicellular tumor spheroids (MTSs, about 100 μm in diameter) were built as 3D in vitro tumor models to evaluate penetrating ability of T4-NPs. As illustrated in Figure 2F, confocal laser scanning microscopy (CLSM) images elucidated that after 3 h incubation with activated T4-NPs, apparent NIR fluorescence (red) was observed even in the center of the MTSs, and the effect was comparable with that induced by T4-PNPs, while only a slight NIR signal was observed on the rim of the MTSs incubated with unactivated T4-NPs. Taken together, amidization of the TAT lysine residues to succinyl amides could efficiently block their nonspecific interactions, while the rapid hydrolysis of the amides at pH 5.0 condition mimicking acid organelles (endo/lysosomes) exactly enabled the efficient activation and exposure of the fully functionalized TAT.

Encouraged by the outstanding extracellular-activated properties, the intracellular delivery and distribution of T4-NPs were inspected by CLSM. After co-culture of 4T1 cells with T4-NPs for 1 h (Figure 3A), T4-NPs were found initially to be entrapped into the acidic organelles such as endosomes

and lysosomes, as evidenced by the overlap of red fluorescence and green fluorescence with Pearson's correlation coefficient calculated to be as high as 0.93. This manifested that T4-NPs entered the cells mainly through endocytic pathway into endo/lysosomes, where SA-TAT could hydrolyze and regenerate TAT. Upon extending of incubation time to 6 h, the Pearson's correlation coefficient was reduced to 0.62, indicating effective escape of T4-NPs from the endo/lysosomes, which might benefit from the prominent penetration nature of TAT on biological membrane systems. Whereafter, the nuclear targeting delivery of T4-NPs was examined. As depicted in Figure 3B, few T4-NPs were observed in the nuclei after a short incubation time of 1 h. More T4-NPs were internalized into the cells and traversed to the perinuclear regions when the incubation time was prolonged to 6 h. Attractively, a large number of T4-NPs were found punctuated on the nuclear membranes and some even successfully penetrated into nuclei after a longer incubation of 12 h. Furthermore, photostability test showed that T4-NPs possessed high photobleaching resistance, which is of vital significance for phototheranostic agents (Figure S5, Supporting Information). Subsequently, the light-induced photodynamic tumoricidal activity of T4-NPs toward 4T1 tumor cells was investigated by CCK-8 assay (Figure 3C). T4-NPs were found no obvious toxicity to 4T1 cells even at a high concentration under dark, indicating good biocompatibility. Upon white light irradiation (24 mW cm^{-2}, 20 min), the profiles of cell viability versus T4 concentration manifested that T4-NPs had an ultra-high tumoricidal efficacy to 4T1 cells with an IC_{50} value (the concentration causing 50% growth inhibition) as low as 7.2 μg mL^{-1}. Aiming to demonstrate phototherapeutic effect of T4-NPs intuitively, fluorescein diacetate/propidium iodide (FDA/PI) double staining protocol was utilized to distinguish live (in green color) and dead (in red color) 4T1 cells (Figure 3D). As expected, strong green fluorescent signal was observed in light irradiation alone and NPs incubation alone groups, indicating low side effect of irradiation itself and desirable biocompatibility of NPs. Attractively, almost all the T4-NPs loaded 4T1 cells presented death state after white light irradiation, strongly suggesting both the excellent photoablation ability and outstanding controllability against cancer cells of T4-NPs. In addition, the intracellular ROS generation was indicated by DCFH-DA as well. As displayed in Figure 3E, 4T1 cells treated with T4-NPs plus white light irradiation aroused bright green fluorescence, while almost no obvious fluorescence was observed in control groups, indicating that ROS can be efficiently generated in live cells, which gave rise to the high phototoxicity of T4-NPs against 4T1 cells. In order to better elucidate the cell killing mechanism of T4-NPs, the apoptosis test using Annexin V-APC/PI detection assay was carried out. FACS analysis revealed that 66.8% 4T1 cells were introduced to apoptosis after treatment with T4-NPs plus white light irradiation, and 14.8% cells were guided to necrosis, yet negligible apoptosis or necrosis was observed in other control groups (Figure 3F). Overall, the T4-NPs succeeded in acid-triggered nucleus-targeted delivery and ultra-strong PDT effects on 4T1 tumor cells.

After demonstrating the superb performance in vitro, the in vivo application feasibility of T4-NPs was further estimated. Initially, we used a fluorescent imaging system for small animals to assess the NIR FLI ability and biodistribution of T4-NPs on 4T1 tumor-bearing BALB/c nude mice by intravenous injection. As illustrated in Figure 4A, the NIR fluorescent signals were distinctly observed in the tumor site at a short monitoring time of 3 h postinjection, indicating the prominent accumulation of T4-NPs in tumor tissue driven by EPR effect. As time goes on, the fluorescent intensity of tumor region enahnced continuously and came to a head at 12 h postinjection, and declined afterward attributing to the metabolism (Figure 4B). Thus, 12 h was chosen as the optimal time point of light irradiation for subsequent PDT. In order to further investigate the biodistribution

of T4-NPs, the treated mice were sacrificed after 24 h injection, and the tumor and main organs were harvested for ex vivo NIR FLI (Figure S6, Supporting Information). It turned out that the tumor tissue exhibited distinct fluorescent signals despite obvious signals were also found in the metabolic organ of liver. Moreover, closer quantitative analysis of the fluorescent intensity in various organs also substantiated this result (Figure 4C). We next assessed the in vivo tumoricidal efficacy of T4-NPs using the same tumor model through systemic administration. Meanwhile, mice administrated with T4-NPs without light irradiation or saline with/without light irradiation served as the controls. Tumor growth curves in Figure 4D showed that the tumor volumes in these control groups increased rapidly during the study period and no significant difference was noticed among them, implying light irradiation alone or T4-NPs administration alone had no suppression effect on tumor growth. Gratifyingly, T4-NPs with light irradiation resulted in remarkable tumor growth inhibition and the average tumor volume at day 15 was less than one-third of the size in saline-administrated group, which was attributed to the precise nuclear targeting and enough ROS generation. After complete treatment of 15 d, all mice were sacrificed and the tumors were collected for weighing. The result further demonstrated the highly effective PDT of T4-NPs with a tumor inhibition rate as high as 78% (Figure 4E). To get a direct insight into the therapeutic mechanism, the exfoliated tumors after different treatments were examined by histological and immunohistochemical analyses (Figure 4F). Hematoxylin and eosin (H&E) staining of tumor sections uncovered that efficient ROS generation capacity as well as precise nuclear-targeting ability based on T4-NPs could induce the extensive destruction of tumor tissues and significant abnormality of tumor cells with many void spaces and conspicuous karyopyknosis, on the contrary, the superabundant and densely arranged tumor cells were obviously visualized in the tumors of control groups. TUNEL immunofluorescence staining assay further verified severe cell apoptosis in the tumor tissue of mice treated with T4-NPs plus white light irradiation. The immunohistochemical studies also disclosed that few Ki67-positive proliferating cells and CD31-positive new microvessels were observed in the irradiated T4-NPs group, unlike massive proliferating cells and neovessels in other control groups, which was in accordance with the TUNEL staining results. In light of the safety importance of theranostic agents in biomedical application, the potential systemic toxicity of T4-NPs was also carefully checked. The body weights of all the treated mice were monitored every three days during the therapeutic process, and reasonable weight changes within normal range were discovered for each group (Figure 4G). Besides, the serum biochemical and hematological parameters were evaluated on healthy BALB/c mice administrated with T4-NPs at a T4 dose of 10 mg kg^{-1} intravenously (Figure S7, Table S2, Supporting Information). Compared with the saline-administered group, the blood biochemistry indexes of hepatic function markers (ALT, AST and ALB) and renal function markers (CR, UA and BUN), as well as routine blood indexes in the T4-NPs-administered group appeared to be normal and the difference was not statistically significant, indicating no obvious systemic side effects of T4-NPs. Moreover, the good biocompatibility of T4-NPs was also obviously revealed by no noticeable organ damage or inflammatory lesions in the H&E-stained slices of major organs after administration with T4-NPs for one week (Figure S8, Supporting Information). On the other hand, as a kind of optically-controlled theranostics, the therapeutic efficacy of T4-NPs could only be activated by light irradiation, which further favored the low systemic toxicity. All these results convincingly demonstrated that T4-NPs with favorable biosecurity well performed in actual phototheranostic applications in terms of NIR FLI-guide PDT.

Conclusions

In summary, we reported here a tumor lysosomal acidity-activated nucleus-targeted phototheranostic system constructed from finely engineered AIE PS and well tailored nanovehicle allowing precise and efficient FLI-guided photodynamic cancer therapy. Four homologous AIEgens with the same backbone were elaborately designed and smoothly synthesized. Their photophysical and chemical properties in terms of absorption, emission and ROS generation can be synchronously boosted towards phototheranostic applications by fine-varying their substituents. Compared with other three AIEgens, TPE-TTMN-TPA bearing the highest structural D-A strength and the most heteroatom components displayed bright NIR fluorescence with the longest emission wavelength, as well as the most prominent ROS production capability, which is even far superior to that of Rose Bengal under white light illumination. With the assistance of artfully modified peptide TAT, TPE-TTMN-TPA NPs can be efficiently delivered to tumor site and activated by tumor lysosomal acidity, and nucleus-targeting function was subsequently accomplished. Both in vitro and in vivo experiments strongly demonstrated that the presennted AIE NPs sharing excellent photostability and good biocompatibility well performed in NIR FLI-guided PDT for cancer treatment affording accurate tumor imaging and effective tumor elimination with a inhibition rate as high as 78%, thus fully representing precise and efficient phototheranostics. This study thus not only provides useful insights into designing superior AIE PSs, but also offers new perspectives for buliding advanced phototheranostic systems by fully exerting the synergistic functions of theranostic cargos and transporting vehicles. This successful example of phototheranostics construction will stimulate the development of more efficient theranostic agents for potential clinical applications.

Experimental Section

The detail experimental processes are available in the Supporting Information.

Acknowledgements

Z.Z. and W.X contributed equally to this work. This work was supported by the National Natural Science Foundation of China (51903163, 21801169, 21788102), the China Postdoctoral Science Foundation Grant (2019M653036), the Natural Science Foundation for Distinguished Young Scholars of Guangdong Province (2020B1515020011), and the Science and Technology Foundation of Shenzhen City (JCYJ20190808153415062, JCYJ20190808121417291). The authors are grateful to the Instrumental Analysis Center of Shenzhen University. All animals operations complied with the protocols approved by the Administrative Committee on Animal Research in Shenzhen Graduate School, Peking University.

Conflict of Interest

The authors declare no conflict of interest.

Received: ((will be filled in by the editorial staff))
Revised: ((will be filled in by the editorial staff))
Published online: ((will be filled in by the editorial staff))

References

[1] K. K. Ng, G. Zheng, Chem. Rev. 2015, 115, 11012.

[2] a) X. Gu, X. Zhang, H. Ma, S. Jia, P. Zhang, Y. Zhao, Q. Liu, J. Wang, X. Zheng, J. W. Y. Lam, D. Ding, B. Z. Tang, Adv. Mater. 2018, 30, 1801065. b) Y. Yuan, C. J. Zhang, M. Gao, R. Zhang, B. Z. Tang, B. Liu, Angew. Chem. Int. Ed. 2015, 54, 1780. c) L. Wu, Y. Sun, K. Sugimoto, Z. Luo, Y. Ishigaki, K. Pu, T. Suzuki, H. Y. Chen, D. Ye, J. Am. Chem. Soc. 2018, 140, 16340.
[3] a) J. Li, K. Pu, Chem. Soc. Rev. 2019, 48, 38. b) X. Ai, J. Mu, B. Xing, Theranostics 2016, 6, 2439.
[4] a) M. Gao, F. Yu, C. Lv, J. Choo, L. Chen, Chem. Soc. Rev. 2017, 46, 2237. b) X. Li, J. Kim, J. Yoon, X. Chen, Adv. Mater. 2017, 29, 1606857. c) X. Ma, N. Gong, L. Zhong, J. Sun, X. J. Liang, Biomaterials, 2016, 97, 10.
[5] a) M. Ethirajan, Y. Chen, P. Joshi, R. K. Pandey, Chem. Soc. Rev. 2011, 40, 340. b) A. Reisch, A. S. Klymchenko, Small 2016, 12, 1968.
[6] a) J. Luo, Z. Xie, J. W. Y. Lam, L. Cheng, H. Chen, C. Qiu, H. S. Kwok, X. Zhan, Y. Liu, D. Zhu, B. Z. Tang, Chem. Commun. 2001, 1740. b) J. Mei, N. L. C. Leung, R. T. K, Kwok, J. W. Y, Lam, B. Z. Tang, Chem. Rev. 2015, 115, 11718.
[7] S. Chen, H. Wang, Y. Hong, B. Z. Tang, Mater. Horiz. 2016, 3, 283.
[8] a) F. Hu, S. Xu, B. Liu, Adv. Mater. 2018, 30, 1801350. b) D. Wang, M. M. S. Lee, W. Xu, R. T. K. Kwok, J. W. Y. Lam, B. Z. Tang, Theranostics 2018, 8, 4925.
[9] a) G. Feng, B. Liu, Small 2016, 12, 6528. b) Z. Zhang, W. Xu, M. Kang, H. Wen, H. Guo, P. Zhang, L. Xi, K. Li, L. Wang, D. Wang, B. Z. Tang, Adv. Mater. 2020, 32, 2003210.
[10] a) S. Xu, Y. Yuan, X. Cai, C. J. Zhang, F. Hu, J. Liang, G. Zhang, D. Zhang, B. Liu, Chem. Sci. 2015, 6, 5824. b) W. Wu, D. Mao, S. Xu, S. Ji, F. Hu, D. Ding, D. Kong, B. Liu, Mater. Horiz. 2017, 4, 1110. c) X. You, H. Ma, Y. Wang, G. Zhang, Q. Peng, L. Liu, S. Wang, D. Zhang, Chem. Asian J. 2017, 12, 1013. d) C. Gui, E. Zhao, R. T. K. Kwok, A. C. S. Leung, J. W. Y. Lam, M. Jiang, H. Deng, Y. Cai, W. Zhang, H. Su, B. Z. Tang, Chem. Sci. 2017, 8, 1822.
[11] A. L. Vahrmeijer, M. Hutteman, J. R. van der Vorst, C. J. H. van de Velde, J. V. Frangioni, Nat. Rev. Clin. Oncol. 2013, 10, 507.
[12] a) M. Ethirajan, Y. Chen, P. Joshi, R. K. Pandey, Chem. Soc. Rev. 2011, 40, 340. b) K. Han, W. Y. Zhang, J. Zhang, Q. Lei, S. B. Wang, J. W. Liu, X. Z. Zhang, H. Y. Han, Adv. Funct. Mater. 2016, 26, 4351.
[13] C. P. Satori, M. M. Henderson, E. A. Krautkramer, V. Kostal, M. M. Distefano, E. A. Arriaga, Chem. Rev. 2013, 113, 2733.
[14] a) W. H. Chen, G. F. Luo, X. Z. Zhang, Adv. Mater. 2019, 31, 1802725. b) P. Gao, W. Pan, N. Li, B. Tang, ACS Appl. Mater. Interfaces 2019, 11, 26529.
[15] L. Pan, J. Liu, J. Shi, Chem. Soc. Rev. 2018, 47, 6930.
[16] V. P. Torchilin, Nat. Rev. Drug Discov. 2014, 13, 813.
[17] a) K. Glunde, S. E. Guggino, M. Solaiyappan, A. P. Pathak, Y. Ichikawa, Z. M. Bhujwalla, Neoplasia 2003, 5, 533. b) C. Ju, R. Mo, J. Xue, L. Zhang, Z. Zhao, L. Xue, Q. Ping, C. Zhang, Angew. Chem. Int. Ed. 2014, 53, 6253.
[18] a) M. Kang, C. Zhou, S. Wu, B. Yu, Z. Zhang, N. Song, M. M. S. Lee, W. Xu, F. J. Xu, D. Wang, L. Wang, B. Z. Tang, J. Am. Chem. Soc. 2019, 141, 16781. b) W. Xu, M. M. S. Lee, J. J. Nie, Z. Zhang, R. T. K. Kwok, J. W. Y. Lam, F. J. Xu, D. Wang, B. Z. Tang, Angew. Chem. Int. Ed. 2020, 59, 9610.
[19] W. Zhao, Z. He, J. W. Y. Lam, Q. Peng, H. Ma, Z. Shuai, G. Bai, J. Hao, B. Z. Tang, Chem 2016, 1, 592.

[20] a) A. D. Frankel, C. O. Pabo, Cell 1988, 55, 1189. b) S. Asoh, S. Ohta, Adv. Drug Deliv. Rev. 2008, 60, 499. c) L. Y. Y. Chou, K. Ming, W. C. W. Chan, Chem. Soc. Rev. 2011, 40, 233.
[21] A. Chauhan, A. Tikoo, A. K. Kapur, M. Singh, J. Control. Release 2007, 117, 148.
[22] E. Jin, B. Zhang, X. Sun, Z. Zhou, X. Ma, Q. Sun, J. Tang, Y. Shen, E. Van Kirk, W. J. Murdoch, M. Radosz, J. Am. Chem. Soc. 2013, 135, 933.
[23] a) P. Xu, E. A. Van Kirk, Y. Zhan, W. J. Murdoch, M. Radosz, Y. Shen, Angew. Chem. Int. Ed. 2007, 46, 4999. b) J. Z. Du, T. M. Sun, W. J. Song, J. Wu, J. Wang, Angew. Chem. Int. Ed. 2010, 49, 3621.
[24] S. S. Han, Z. Y. Li, J. Y. Zhu, K. Han, Z. Y. Zeng, W. Hong, W. X. Li, H. Z. Jia, Y. Liu, R. X. Zhuo, X. Z. Zhang, Small 2015, 11, 2543.

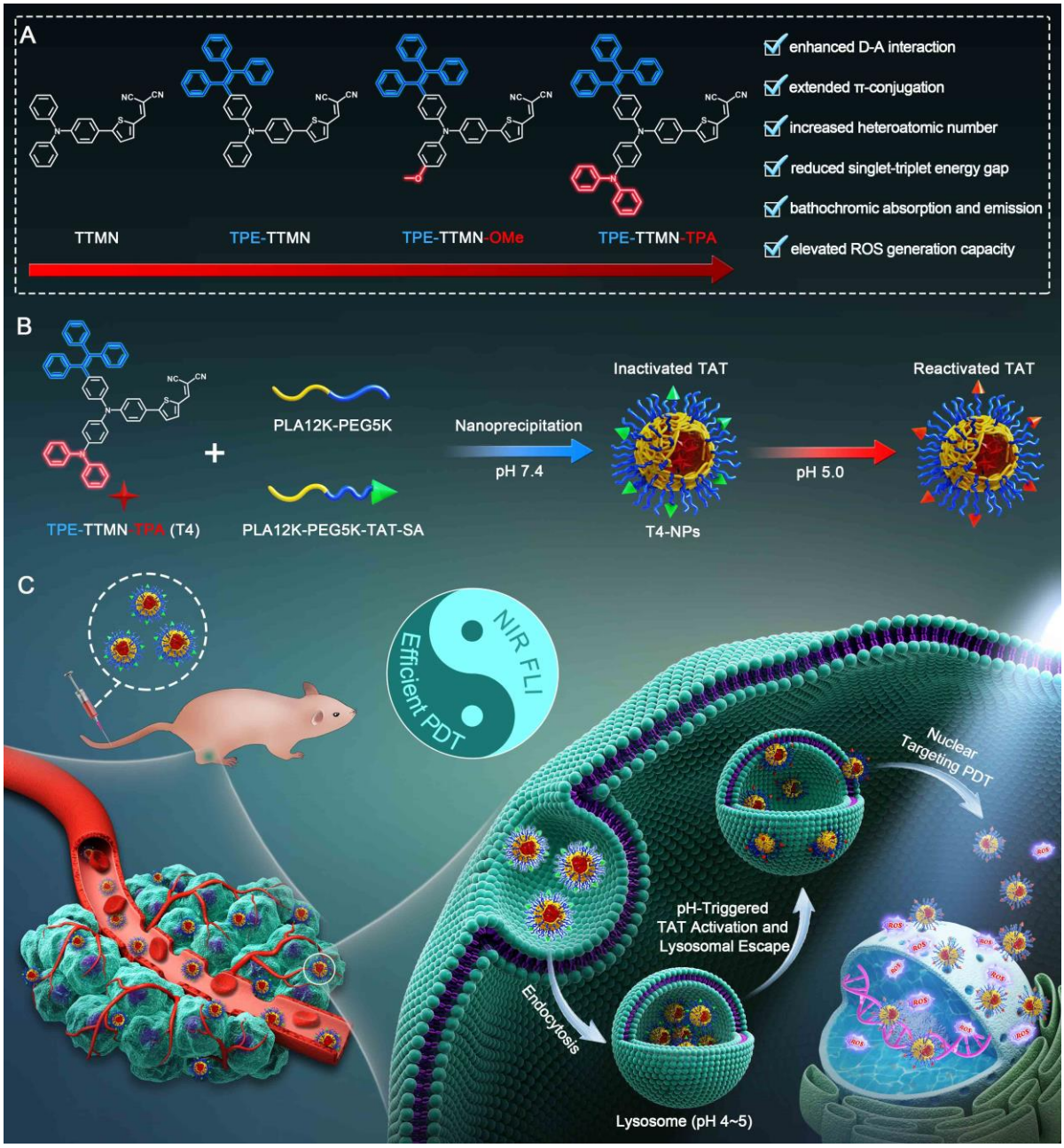

Scheme 1. Schematic illustration of molecular structures, nanofabrication, acid-activated behaviors and nucleus-targeted phototheranostic application. A) Molecular structures of rationally designed AIEgens. B) Preparation procedure of T4-NPs and acid-triggered activity recovery of TAT. C) Illustration of acid-triggered nucleus-targeted cancer theranostics by means of NIR FLI-guided precise photodynamic therapy.

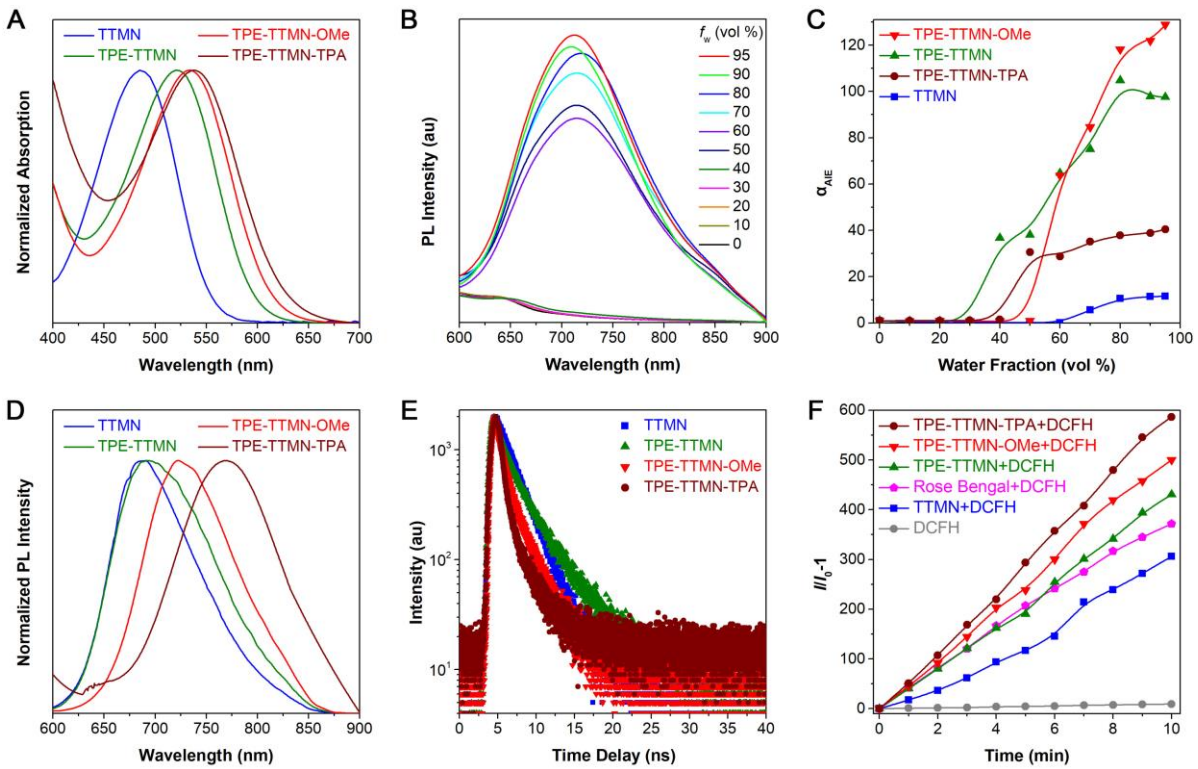

Figure 1. Photophysical and photodynamic properties of TTMN, TPE-TTMN, TPE-TTMN-OMe and TPE-TTMN-TPA. A) Normalized absorption spectra of these four AIEgens in the ACN solution. B) PL spectra of TPE-TTMN-TPA (1×10^{-5} M) in ACN/water mixtures with different water fractions (f_w). C) Plots of the relative emission intensity (I/I_0) versus water fraction. I_0 and I are the peak values of fluorescence intensities of AIEgens in ACN and ACN/water mixtures, respectively. D) Normalized PL spectra and E) fluorescence decay curves of the AIEgens in solid state. F) ROS generation of the AIEgens (2×10^{-7} M) upon white light irradiation (22.1 mW cm^{-2}) using dichlorofluorescin (DCFH) as an indicator.

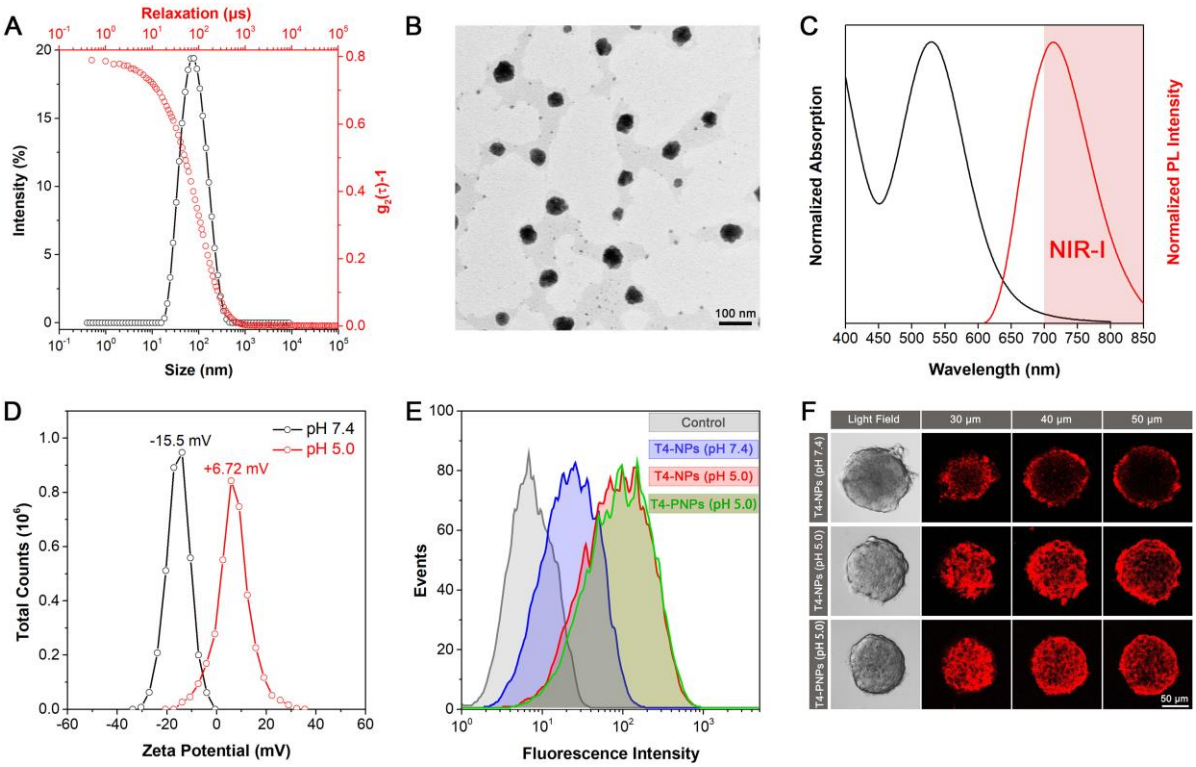

Figure 2. Characteristics and acid-activated behaviors of T4-NPs. A) Size distribution and B) TEM image of T4-NPs in aqueous solutions. C) Normalized absorption and emission spectra of T4-NPs in aqueous solutions. D) Zeta potentials of T4-NPs after incubation for 24 h at pH 7.4 and 5.0, respectively. E) FACS analysis for quantitative cellular uptake into 4T1 cells and F) CLSM images of 4T1 MTSs after incubation with T4-NPs or T4-PNPs for 3 h at a unified T4 concentration of 5 μg mL^{-1}. These NPs were pretreated at pH 7.4 or 5.0 PBS for 24 h at 37 ºC.

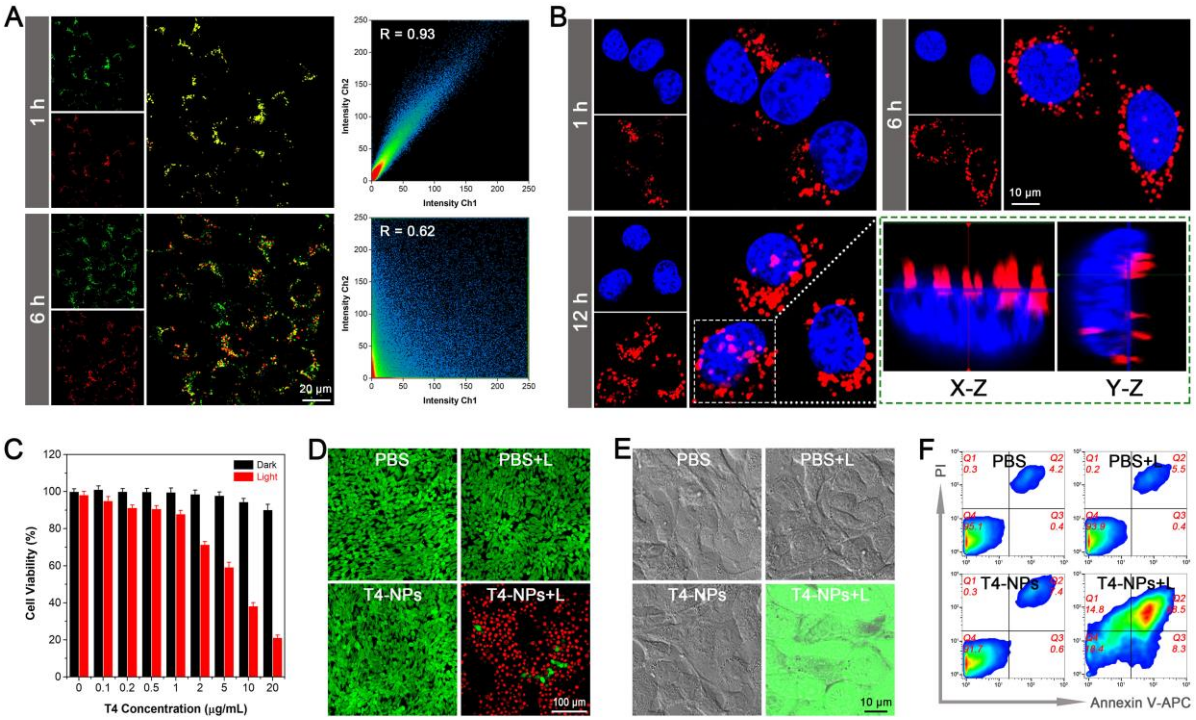

Figure 3. Intracellular tracking and photodynamic tumoricidal effects of T4-NPs on 4T1 tumor cell line. A) CLSM images of 4T1 cells incubated with T4-NPs (5 μg mL^{-1} T4) for different time including LysoTracker-stained lysosome channel (green), T4 channel (red) and overlay images; and scatter plots indicating the overlap coefficient (inset: calculated Pearson's correlation coefficient). B) CLSM images for nucleus-targeted delivery of T4-NPs (5 μg mL^{-1} T4) with various monitoring time points including Hoechst 33342-stained nucleus channel (blue), T4 channel (red) and overlay images; and magnified cell for the visualization of nuclear penetration from different lateral views. C) Cell viability of 4T1 cells incubated with T4-NPs for 48 h determined by CCK-8 assay in dark condition or under white light irradiation (mean ± SD, n = 6). D) Live/dead cell staining of 4T1 cells treated with PBS, PBS plus light (PBS + L), T4-NPs, and T4-NPs plus light (T4-NPs + L). Concetration: 20 μg mL^{-1} T4. E) Intracellular ROS level of 4T1 cells after treatment with various formulations. F) Apoptosis analysis of 4T1 cells induced by various formulations using Annexin V-APC/PI detection assay by FACS.

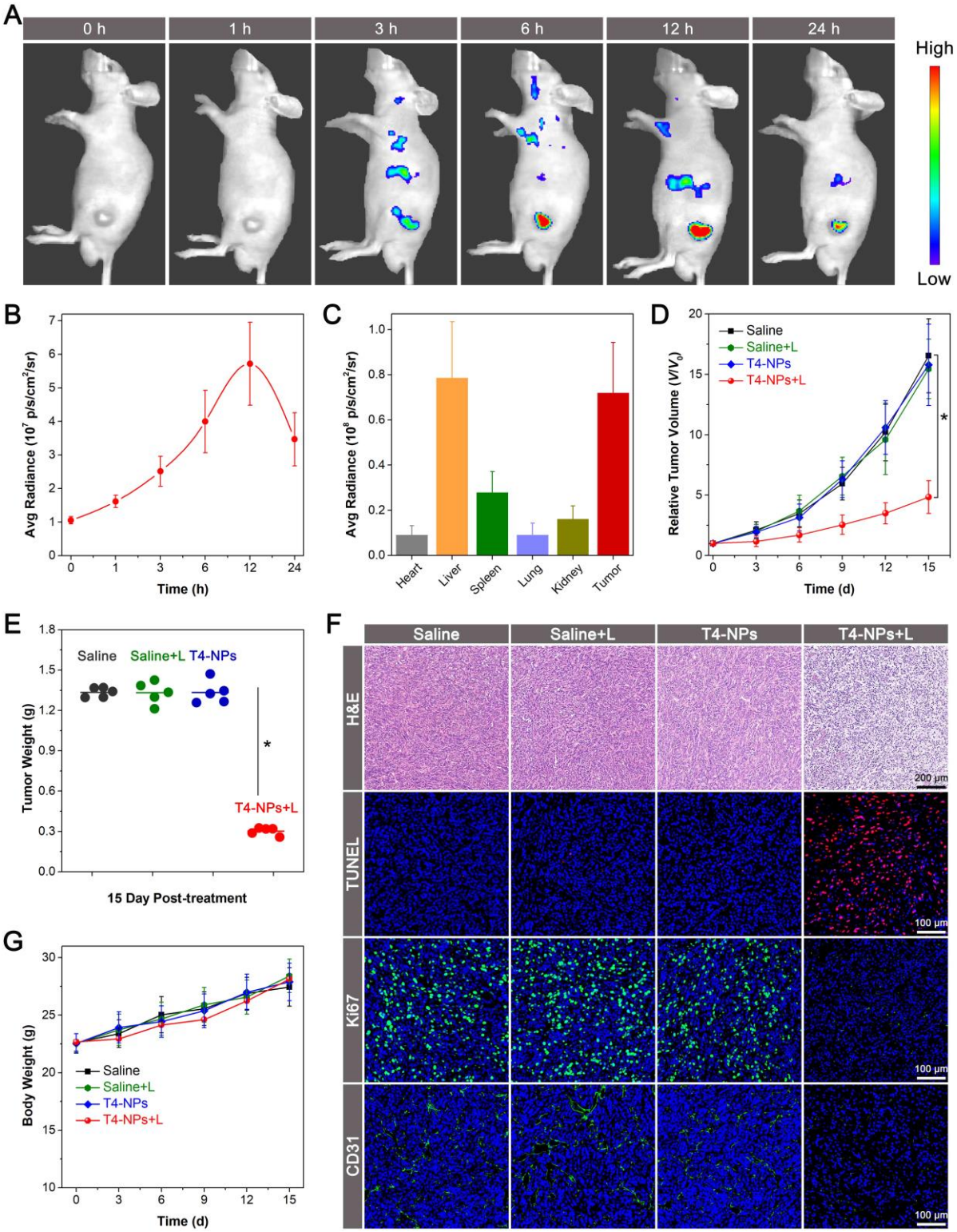

Figure 4. In vivo NIR FLI-guided PDT assessment of T4-NPs on 4T1 tumor-bearing BALB/c nude mice through systemic administration. A) NIR FLI of mice and B) quantitative fluorescent curve of tumor tissues at different monitoring time after intravenous injection of T4-NPs (10 mg T4 kg^{-1}). C) Quantitative fluorescent intensities of tumor tissue and major organs at 24 h postinjection. D) Time-dependent tumor growth curves of tumor-bearing mice with various treatments (n = 5, $*p < 0.001$). E) Tumor weights of mice after various treatments for 15 d. F) H&E, TUNEL, Ki67, and CD31 staining analyses of tumor tissues at day 15 after treatments. TUNEL-positive cells, Ki67-positive

cells and CD31-positive vessels were stained in red, green and green, respectively. G) Body weight changes of mice with different treatments over 15 d.

Entry fot the Table of Contents

An acid-triggered nucleus-targeted phototheranostic agent based on finely engineered AIE PS and well tailored nanodelivery system was constructed for the first time allowing precise and efficient NIR FLI-guided photodynamic cancer therapy.

Keywords: aggregation-induced emission, photodynamic therapy, NIR emission, molecular engineering, nucleus-targeted theranostics

Zhijun Zhang, Wenhan Xu, Peihong Xiao, Miaomiao Kang, Dingyuan Yan, Haifei Wen, Nan Song, Lei Wang, Dong Wang,* and Ben Zhong Tang*

Precise and Efficient Phototheranostics: Molecular Engineering of Photosensitizers with Near-Infrared Aggregation-Induced Emission for Acid-Triggered Nucleus-Targeted Photodynamic Cancer Therapy